Microwave Drying of Softwood in an Oversized Waveguide: Theory and Experiment

Patrick Perré
ENGREF—Laboratory of Forest Sciences, Forest Products Team, F-54042 Nancy Cedex, France

Ian W. Turner
School of Mathematics, Queensland University of Technology, Brisbane, Q4001, Australia

A comparison between experimental and theoretical results for the combined microwave and convective drying of softwood is presented. The microwave applicator used for the experiments was an oversized waveguide, and the results for both sapwood and heartwood were analyzed. To elucidate on the physics of the process at a fundamental level, a complete model is proposed, which considers the intricate link that transpires between the heat- and mass-transfer phenomena and the power distribution throughout the sample during drying. The resulting model, which uses a comprehensive 2-D set of equations to describe the drying process, together with a complete 3-D solution of the Maxwell equations within the waveguide in the time domain, can be used to investigate many aspects of dielectric drying. This research deals with the spatial variation of the power density within the material at various drying times and the effect of the anisotropy of the transfer properties on the shape and evolution of the power distribution. Most importantly, it focuses on the prediction of the location of hot spots and thermal runaway within the sample from the viewpoint of product quality. Strengths and weaknesses of the model are highlighted.

Introduction

In previous research relating to combined microwave and convective drying processes (Constant, 1992; Constant et al., 1996; Jolly and Turner, 1991; Perré, 1995; Turner and Jolly, 1990, 1991) comprehensive *one-dimensional* mathematical models were postulated and investigations were undertaken for isotropic porous media, such as brick and Ytong light concrete, as well as for anisotropic media, such as wood. The results of those research efforts clearly demonstrated the effectiveness of combining dielectric heating methods with classical convective drying processes, and the general conclusions of the work indicated that substantial differences exist between convective drying and the microwave enhanced case. The main differences, and perhaps the one that generated the most interest with this particular drying strategy, was the significant reduction in product drying times together with the high drying rates that can be achieved with the use of microwave energy. In fact, for isotropic materials such as brick and Ytong cement, drying times two to three times faster than convective drying were obtained; however, this reduction in drying time was found to be dependent on numerous issues, including the amount of microwave incident power used for the drying process, the type of product being dried, the applicator used to propagate the electromagnetic energy, and the dimensions of the product.

Other important conclusions drawn from those studies included the identification of the following heat and mass transport phenomena:

Evidence of Volumetric Heating. Because the electromagnetic fields couple very well with the liquid that is distributed throughout the wet material, as a direct result of the high dielectric loss factor of water, a bulk heating phenomenon prevails throughout the product.

Evolution of Internal Product Temperatures Exceeding the Boiling Point of Water and, Consequently, Inducing a Large Internal Pressure Buildup. A pumping effect, due to the high internal vaporization, accelerates the liquid migration mechanisms that evolve within the product during drying. However,

Correspondence concerning this article should be addressed to I. W. Turner.

as a direct result of the elevated temperatures and pressures generated, there is a greater risk of product degradation.

Existence of Large Liquid and Vapor Fluxes Directed from the Interior of the Material Toward the Drying Surface. During the period when the microwave power absorption maximizes within the material, large liquid and vapor fluxes can be observed exiting through the product surfaces. This phenomenon underlines the importance of using an adequate air-flow rate over the drying surface in order to avoid excess liquid accumulation.

Evidence of Preferential Heating of Wetter Areas in Thick Materials, Together with a Moisture Leveling. The power-density distribution appears to track, and subsequently heat and evaporate the liquid in the wetter areas of the material, causing a moisture leveling effect within the product.

Presence of Large Thermal Gradients Stretching from the Interior to the Exterior of the Material. Due to the fact that the surface of the material is often cooled by evaporation during microwave heating, the resulting thermal gradients that are established within the material can also help accelerate the drying process.

Unfortunately, while the preceding advantages of microwave-enhanced drying are now well known, it still seems that this technology has not been accepted as a viable option within the industrial drying sector. Perhaps one of the largest encumbrances in the advancement of the technology is the lack of knowledge regarding the exact coupling that arises between the material and the microwave configuration during the heating process. This gap between theory and practice motivates the need for more advanced fundamental modeling of these types of drying processes so that an improved understanding of the underlying physics can be ascertained, and consequently the technology advanced further. Here, a complete model is derived that combines the power of a very well-established two-dimensional heat- and mass-transfer model known as *Transpore* with a rigorous three-dimensional calculation of the electromagnetic fields in order to deduce the power-density distribution within the material being heated.

The capabilities of the simulation code *Transpore* are already well documented in the literature where it has been tested for a number of drying configurations, including convective drying at high temperatures; microwave drying; infrared drying; contact heating until boiling occurs; for a wide variety of different materials such as softwood, light concrete, paper, and granular porous media (Perré and Degiovanni, 1990; Perré et al., 1993; Perré and Turner, 1996). The electromagnetic code has been used previously to study numerous microwave heating processes in a variety of microwave applicator configurations such as waveguides and cavities (De Pourcq, 1985; Liu et al., 1994). In some more recent research, the heating of polymers within ridged waveguides has been studied (Liu and Turner, 1995; Liu et al., 1996). In fact, both the transport and electromagnetic models prove to be very powerful tools for assisting with the identification of important fundamental knowledge pertaining to both drying and dielectric heating processes, and with such knowledge it is possible to guide future experimental research in this field.

The material chosen for investigation in this research is softwood. This type of material represents a good test for the numerical computations since wood is highly anisotropic, with the liquid and gas permeabilities exhibiting an anisotropy ratio as high as 1,000 across the radial (R) and longitudinal (L) directions of the board. Further, the aspect ratios in the dimensions of the $R-L$ plane can be large, with typical ratios being anywhere between 1:10 and 1:50. Most importantly, however, the system of macroscopic equations that describes the wood-drying process has discontinuities within the transport coefficients at critical points in the drying process. All of these factors provide a difficult challenge for the numerical analyst—from the selection of the best discretization method, to the choice of the most efficient inner and outer iteration strategies that are necessary to resolve such an intricately coupled and highly nonlinear set of equations. In this work the structured mesh control volume method is used for the discretization of the transport equations and Newton outer iteration, combined with the biconjugate gradient stabilized inner iteration solver with an incomplete LU decomposition preconditioner, is used to advance the nonlinear algebraic system in time (Turner and Perré, 1996).

The aim of this work is to demonstrate that numerical simulation can be used to assist with the design of microwave applicators that can ultimately lead to a process-control strategy that can provide an efficient and uniform microwave drying process.

Experimental Configuration

The experiments that were carried out in order to analyze the combined microwave and convective drying of softwood in a small-scale oversized waveguide, were performed at the Laboratoire de Physico-Chimie Industrielle, Nancy, France (see Figures 1 and 2). The experimental apparatus used to perform the experiments on wood is basically the same as the one used for analyzing the combined microwave and convective drying of light concrete. The exact dimensions of the experimental configuration can be found elsewhere (Constant, 1992; Constant et al., 1996).

The oversized waveguide system exhibited in Figure 1 operates by propagating traveling waves along the z-direction of the waveguide toward a water load that is situated at the end of the guide. The water load ensures that only a minimal amount of energy is reflected back to the sample, while an

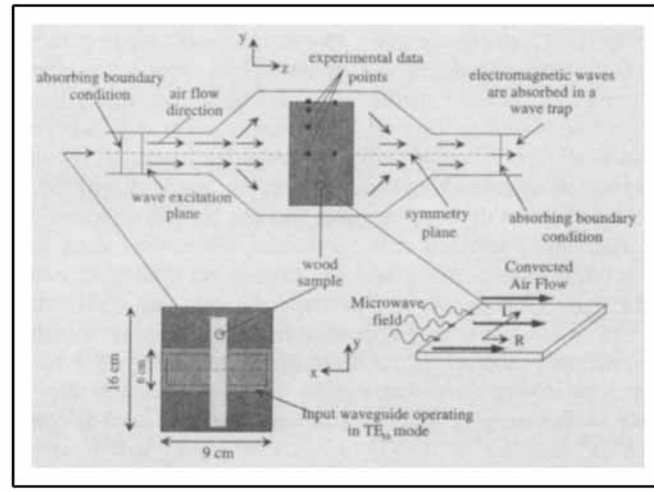

Figure 1. Oversized waveguide used for this analysis.

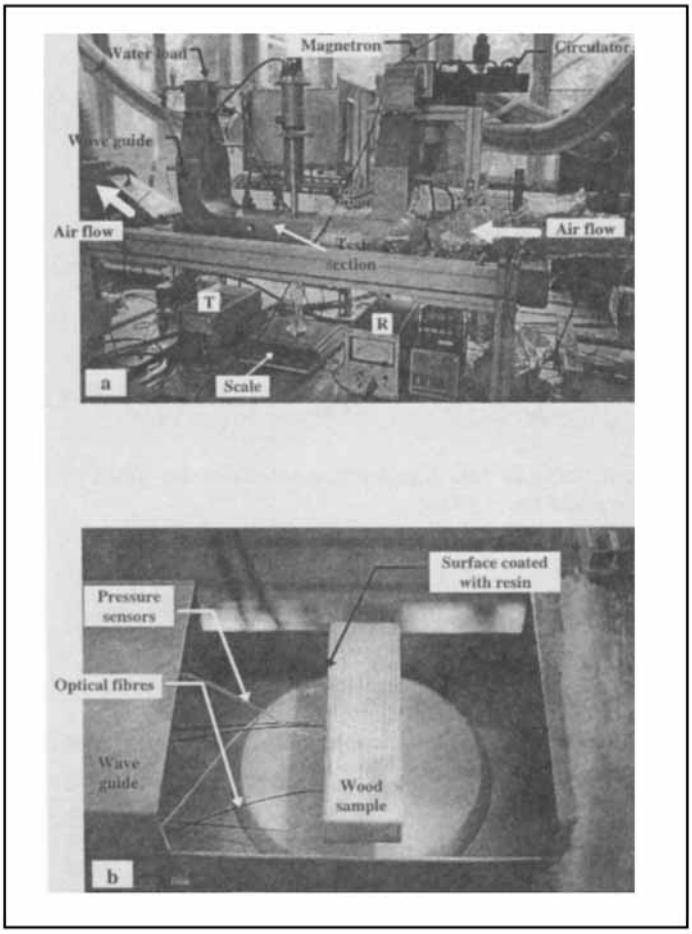

Figure 2. (a) Actual experimental configuration; (b) wood sample located in the oversized waveguide section of the dryer.

R, T = measurement of reflected and transmitted power, respectively.

isocirculator, which is located at the front end of the guide, is used to trap any energy reflected from the sample damaging the magnetron. The material, in this case a sample of wood, is inserted in the central oversized section of the guide. As the microwave heating proceeds, the material absorbs a certain amount of energy from the exponentially decaying traveling microwave field in accordance with the properties of the effective loss factor.

Typically, for wood, large variations in the properties can be observed between different species, different trees of the same species, and even at different locations within the same tree. With respect to drying, the most commonly known difference lies between sapwood and heartwood, where it has been found that heartwood has much smaller transfer properties and a lower initial moisture content than sapwood. Furthermore, the drying of wood can be studied only for green boards. Indeed, the behavior of a board that has been previously dried and then resaturated, is often very different from the characteristics observed during the first drying cycle for a green board. All of these facts are of high importance for the experiments.

The wood samples used for the experiments originated from trees that were freshly felled in a forest belonging to ENGREF. The cutting pattern is well documented (see, for example, Perré and Turner, 1996), so that it is possible to know the exact location of each board within the log. Great care must be taken up to the time the experiments are performed. During the preparation, the boards are coated with an impervious film in order to avoid drying. It should be noted that for the tests performed here, unlike that reported previously for high-temperature convective drying experiments (Perré et al., 1993), it was not possible to measure the internal temperatures and pressures of the wood at exactly the same locations. In fact, as a direct consequence of the electromagnetic field, very few materials can be used to assist with the experimental measurements. In this work only inert materials, such as glass and Teflon, and materials with dielectric properties much less than those of wood, such as silicone and epoxy resin, were used.

Just prior to the experiments, holes were drilled at the desired locations where the temperature and pressure sensors were to be placed within the wood sample. At first, a deep hole with a small diameter was drilled ($\phi \approx 2$ mm, $L \approx 30$ mm), followed by a larger hole with a smaller depth ($\phi \approx 6$ mm, $L \approx 5$ mm). In order to avoid leakage during the test, silicon tubes were inserted inside the larger holes and the entire face of the sample, including the tubes, were coated with epoxy resin. Next, the samples were put into impervious bags and placed in a climate chamber at 40°C to accelerate the hardening of the resin glue. The samples remained in the bags until they were required for the drying tests.

Immediately before the experiment commenced, the waveguide incident power was calibrated without the sample inside. In this way, all of the magnetron power was absorbed by the water load situated at the end of the waveguide, so that the power meter, which measures the reflected power (label ***R*** in Figure 2a), indicated zero and the meter that measures the transmitted power (refer to label ***T*** in the same figure) indicated the total power of the magnetron. Finally, the optical fibers of the thermometer and the Teflon tubes were connected to the pressure gauges and inserted into the holes. The silicon tubes that seal the fibers and Teflon tubes were used to ensure the sample was airtight.

During the experiment, the weight of the sample, the temperature of the wood at three locations, the internal pressure at two locations, the transmitted power, the reflected power, the power absorbed by the sample, the air temperature, and the humidity within the chamber were collected by a data logger that was connected to a personal computer.

There are two important assumptions that must be discussed before the development of the mathematical model can be presented succinctly in the following section. First, the entrance and exit standard TE waveguide sections, which are used to direct electomagnetic energy into and out of the central oversized heating section of the small-scale microwave dryer, were actually L-shaped in design (see Figure 2a). The curved sections of these guides were not modeled in this work. Instead, it was assumed that the dominant TE_{10} mode prevailed throughout the entire entrance and exit L-shaped guide regions. The use of an input plane, which excites only the single mode in the shortened entrance rectangular guide section shown in Figure 1, together with absorbing boundary planes at both ends of the configuration (again see Figure 1), which simulate, respectively, the circulator and wave trap connected at either end of the dryer, ensure that reality is

represented adequately. Second, the wood sample had the entire xy-plane of the trailing edge located closest to the wave trap coated with a resin glue (Figure 2b). Such a setup ensured that the internal pressure gauges could be sealed airtight within the sample. This resin layer guaranteed that accurate pressure and temperature measurements could be recorded throughout drying.

Fortunately, the loss factor change with temperature of this resin was low enough to make it sufficiently transparent to microwave energy, thus allowing its effect on the drying process to be neglected. Unfortunately, the use of this resin caused the trailing edge of the sample to become impermeable to mass flow, and in order to capture the real three-dimensional drying phenomena that were evident during the drying process, while still maintaining a two-dimensional drying model that simulated the process within acceptable computational times, a drying flux boundary condition was imposed at the rear boundary of the wood sample.

Mathematical Formulation

In this work, Maxwell's electromagnetic equations are coupled to an existing comprehensive two-dimensional heat- and mass-transfer model (Transpore), and the microwave-enhanced convective drying of softwood is studied both experimentally and numerically. The solution of the Maxwell equations is performed in the time domain by using the finite difference time-domain (FD-TD) technique (Liu et al., 1993; Liu and Turner, 1995). The combination of the Transpore and FD-TD models allows, for possibly the first time, the complete mathematical description of the microwave heating phenomena evolving within the wood sample that is located inside the oversized waveguide exhibited in Figure 1. In this section the various components of each model are detailed.

Transport model

The wood drying process can be defined by a set of three state variables whose exact definitions may change at different stages of drying. The model described here endeavors to identify and subsequently track when these changes of state occur, so that the appropriate set of system variables can be utilized within the model. The resulting simulation code, which is developed directly from the mathematical description, allows the evolution of the distributions of these state variables to be analyzed throughout the drying process.

The main transport mechanisms that enable moisture movement during the drying of wood are liquid flow due to capillary, diffusing water vapor, vapor convection in bulk gas flow, bound liquid diffusion, and liquid flow in response to the gradient of gaseous pressure. The macroscopic conservation equations governing the heat- and mass-transfer phenomena that arise in softwood during the drying process are now well known (Whitaker, 1977; Perré and Turner, 1996; Turner, 1996). These equations are summarized below:

Liquid conservation

$$\frac{\partial}{\partial t}\left(\phi S_w \rho_w + \phi S_g \rho_v + \bar{\rho}_b\right) + \nabla\cdot\left(\rho_w \bar{v}_w + \rho_v \bar{v}_g + \overline{\rho_b v_b}\right) = \nabla\cdot\left(\rho_g \bar{\bar{D}}_{\text{eff}} \nabla\omega_v\right). \quad (1)$$

Energy conservation

$$\frac{\partial}{\partial t}\left(\phi S_w \rho_w h_w + \phi S_g(\rho_v h_v + \rho_a h_a) + \bar{\rho}_b \bar{h}_b + \rho_0 h_s - \phi S_g P_g\right) + \nabla\cdot\left(\rho_w h_w \bar{v}_w + (\rho_v h_v + \rho_a h_a)\bar{v}_g + h_b \overline{\rho_b v_b}\right) = \nabla\cdot\left(\rho_g \bar{\bar{D}}_{\text{eff}}(h_v \nabla\omega_v + h_a \nabla\omega_a) + \bar{\bar{K}}_{\text{eff}} \nabla T\right) + \Phi. \quad (2)$$

Air conservation

$$\frac{\partial}{\partial t}(\phi S_g \rho_a) + \nabla\cdot(\rho_a \bar{v}_g) = \nabla\cdot\left(\rho_g \bar{\bar{D}}_{\text{eff}} \nabla\omega_a\right), \quad (3)$$

where the gas- and liquid-phase velocities are given by the *generalized Darcy's law*:

$$\bar{v}_\ell = -\frac{\bar{\bar{K}}_\ell \bar{\bar{k}}_\ell}{\mu_\ell}\nabla\varphi_\ell, \qquad \nabla\varphi_\ell = \nabla P_\ell - \rho_\ell g \nabla\chi \quad (4)$$

where $\ell = w,\ g$; the quantities φ are known as the phase potentials; and χ is the depth scalar.

In order to close this system, the following constraints and constitutive relations are used:

$$S_g + S_w = 1,$$

$$P_g = \frac{\rho_g RT}{M}, \quad P_v = \frac{\rho_v RT}{M_v}, \quad P_a = \frac{\rho_a RT}{M_a},$$

$$P_g = P_v + P_a \quad \text{and} \quad M = M_a + (M_v - M_a)\frac{P_v}{P_g},$$

$$P_w = P_g - P_c(S_w, T). \quad (5)$$

The enthalpy–temperature relations are given by the following definitions:

$$h_s = C_{ps}(T - T_R), \quad h_a = C_{pa}(T - T_R),$$

$$h_v = h^0_{\text{vap}} + C_{pv}(T - T_R), \quad h_w = C_{pw}(T - T_R),$$

$$\bar{h}_b = h_w - \frac{1}{\bar{\rho}_b}\int_0^{\bar{\rho}_b} \Delta h_w \, d\rho, \quad h_b = h_w - \Delta h_w, \quad (6)$$

and the mass fractions of vapor and air in the gaseous phase are given by

$$\omega_v = \frac{\rho_v}{\rho_g} \quad \text{and} \quad \omega_a = \frac{\rho_a}{\rho_g}. \quad (7)$$

Note that the calculation of the vapor pressure inside the medium uses the assumption of local thermodynamical equilibrium. Consequently, $P_v = P_{vs}(T) \times \psi(T, X_b)$, where P_{vs} is the saturated vapor pressure and ψ is a function that is defined according to the sorption curves.

The term Φ within Eq. 2 represents the volumetric heat source that is established due to the dielectric heating mech-

anisms encountered during microwave-enhanced drying processes. When this term is present within the framework of the model, it is necessary to couple the heat- and mass-transfer equations with the Maxwell equations in order to determine the electric-field distribution (Turner, 1991). This volumetric power-density term is given by the following expression:

$$\Phi = \frac{1}{2}\sigma_e |\boldsymbol{E}|^2 \tag{8}$$

where $\boldsymbol{E}$ is the electric field vector, and σ_e is the effective conductivity. It is clear that before the heat- and mass-transfer equations can be resolved entirely, the magnitude of the electric field within the material for the microwave applicator configuration shown in Figure 1 must be determined. Unfortunately, analytical expressions for the power density source term can be derived only for specialized applicator designs, and typically the use of numerical techniques becomes an absolute necessity. The derivation of the numerical solution of Maxwell's equations used in this work is discussed in great detail in the subsection on the electromagnetic model.

Bound Liquid Flux Definition. The driving potential for the bound liquid migration is assumed to be proportional to a gradient in the chemical potential μ_b:

$$\overline{\rho_b \boldsymbol{v}_b} = -\overline{\overline{\boldsymbol{D}}}_b \nabla \mu_b. \tag{9}$$

Stanish et al. (1986), and later Pang et al. (1992) gave a form of the chemical potential that allows the bound liquid flux to be written in terms of gradients in the vapor pressure and the temperature:

$$d\mu_v = -\frac{S_v}{M_v}\cdot dT + \frac{1}{\rho_v}\cdot dP_v$$

$$\overline{\rho_b \boldsymbol{v}_b} = -\overline{\overline{\boldsymbol{D}}}_b (1-\phi)\left(\frac{1}{\rho_v}\nabla P_v - \frac{S_v}{M_v}\nabla T\right). \tag{10}$$

In Eq. 10 the molar entropy S_v is a state function of temperature and vapor pressure. This definition will be adopted for all computations performed in this work.

Physical Properties. Most of the key parameters that exist within the macroscopic equations (Eqs. 1–3) are strongly dependent on the structure of the material. These properties, together with their postulated functional dependencies, are listed in the following paragraphs.

Capillary Pressure. The *capillary pressure* is assumed to be a function of *free* liquid saturation $J(S_w)$ and surface tension $\sigma(T)$. The function J is dependent on the internal structure of the porous material, and for wood may be not only fundamentally different for each species, but may differ even for heartwood and sapwood or earlywood and latewood located within the same tree (Puiggali and Quintard, 1990; Bonneau, 1991; Perré, 1997):

$$P_c(S_w, T) = J(S_w)\sigma(T). \tag{11}$$

In the calculations performed here, the capillary pressure deduced from the pore-size distribution in softwood was found to be well represented by the following functional form:

$$J(S) = \frac{a}{S + 5\times 10^{-3}} - \frac{b}{1.02 - S} + c(1-S) - d, \tag{12}$$

where $a = 3{,}150$; $b = 1047 + 3.368\times\rho$; $c = 149.8\times\rho$; and the parameter d is determined by the constraint that $J(1) = 0$.

The value of ρ used in Eq. 11 should be the density of the wood at 12% moisture content. The correlation, Eq. 12, was obtained by fitting the proposed functional form to the experimental data obtained by using image analysis of anatomical cross sections (Perré, 1997).

Permeabilities. The *relative permeability* correlation is one of the most important in the macroscopic model; however, it is the one parameter that the least is known. It has been shown previously that the use of slightly different functional forms of this parameter can impact substantially upon the results of the computations (Couture, 1995; Turner and Perré, 1995, 1996). In this work, the relative permeability functions summarized in Table 1 will be used for the computations.

Vapor Diffusivity. The *effective diffusivity* tensor is assumed to depend on liquid saturation, pressure, and temperature and is given by the following formula:

$$\overline{\overline{\boldsymbol{D}}}_{\text{eff}}(S_w, T, P_g) = \bar{\bar{f}} \times \bar{\bar{k}}_g(S_w) \times 2.26\times 10^{-5}\left(\frac{T}{T_R}\right)^{1.81}\frac{P_R}{P_g}, \tag{13}$$

where $\bar{\bar{f}}$ is the dimensionless diffusivity tensor, which represents the ratio of diffusivity in wood compared to the one in air.

Thermal Conductivity. In this work the *thermal conductivity* (for softwood) is taken as a linear function of moisture content:

$$\overline{\overline{\boldsymbol{K}}}_{\text{eff}}(X) = \overline{\overline{\boldsymbol{K}}}_0(a + bX), \tag{14}$$

where a and b are constants that depend on the wood species.

The conservation equations just described can be cast succinctly into a generalized form that involves all of the necessary migration mechanisms that allow an adequate description of the evolution of the free-liquid, bound-liquid, and gas phases that coexist within the infrastructure of the porous medium:

Table 1. Relative Permeabilities

Liquid Moisture Content	Relative Permeability of the Liquid Phase	Relative Permeability of the Gas Phase
$X_{wf} = 0$	0	1
Transverse: $0 \le X_{wf} \le X_{\text{sat}}$	$\left(\frac{X_{wf}}{X_{\text{sat}}}\right)^3$	$1 + \left(2\frac{X_{wf}}{X_{\text{sat}}} - 3\right)\left(\frac{X_{wf}}{X_{\text{sat}}}\right)^2$
Longitudinal: $0 \le X_{wf} \le X_{\text{sat}}$	$\left(\frac{X_{wf}}{X_{\text{sat}}}\right)^8$	$1 + \left(4\frac{X_{wf}}{X_{\text{sat}}} - 5\right)\left(\frac{X_{wf}}{X_{\text{sat}}}\right)^4$

After Perré et al. (1993).

$$\frac{\partial \Psi}{\partial t} - \nabla \cdot \boldsymbol{J} = \Phi,$$

where

$$\boldsymbol{J} = \bar{\bar{\boldsymbol{K}}}_1 \nabla \varphi_w + \bar{\bar{\boldsymbol{K}}}_2 \nabla \varphi_g + \bar{\bar{\boldsymbol{K}}}_3 \nabla \omega_v + \bar{\bar{\boldsymbol{K}}}_4 \nabla \omega_a + \bar{\bar{\boldsymbol{K}}}_5 \nabla \mu_b + \bar{\bar{\boldsymbol{K}}}_6 \nabla T. \quad (15)$$

In Eq. 15, the term Ψ represents the conserved quantities of total liquid, energy, or air, where, for example, $\Psi_w = \phi S_w \rho_w + \phi S_g \rho_v + \bar{\rho}_b$. The kinetic tensor terms denoted by $\bar{\bar{\boldsymbol{K}}}_i$ are complicated functions of the state system variables. Note further that not all of the driving potentials given in Eq. 15 are actually present in each of the macroscopic balance equations, nor are they all present for each drying state. Equation 15 will be used as the basis for further discussion in the subsection where the numerical treatment of the transport model is described.

Boundary and Initial Conditions. For the configuration shown earlier in Figure 1, the boundary conditions for the external drying surfaces of the sample must be specified. It is assumed that the driving potentials at these surfaces are of the following form:

$$\boldsymbol{J}_w \cdot \hat{\boldsymbol{n}} = k_m c M_v \ln\left(\frac{1-x_\infty}{1-x_v}\right)$$

$$\boldsymbol{J}_e \cdot \hat{\boldsymbol{n}} = q(T-T_\infty) + \sigma(T^4 - T_\infty^4) + h_v k_m c M_v \ln\left(\frac{1-x_\infty}{1-x_v}\right), \quad (16)$$

where $\boldsymbol{J}_w$ and $\boldsymbol{J}_e$ represent the total liquid and energy fluxes through these boundary surfaces, and x_v and T are, respectively, the molar fraction of the gas vapor and the temperature at the exchange surfaces. The corresponding variables with the subscript 0 indicate quantities that are characteristic of the external drying conditions. The quantities k_m and q are the mass- and heat-transfer coefficients obtainable from the classic *boundary layer theory*. The expression for the external mass flux, which is derived from the *film theory* (Bird et al., 1960), tends to infinity in the case of pure vapor. The singularity causes convergence problems to arise during the numerical simulation, and usually simpler expressions that seek to remain as close as possible to the physics when approaching pure vapor in the gaseous phase are derived from this formulation (Perré and Degiovanni, 1990).

However, in this work, due to the overall philosophy of the Newton–Raphson scheme (Turner and Perré, 1996), it is possible to use directly the original expression (Eq. 16) during the simulations. Note that the radiative heating term is assumed negligible in comparison with the convective term for the investigations carried out here.

The presence at the external drying surfaces is fixed at the atmospheric value:

$$P_g = P_\infty \quad (17)$$

On the symmetry plane, through the center of the material in the *yz*-plane (Figure 1), all fluxes of liquid, vapor, air, and heat are assumed zero.

Initially the porous medium has some prescribed moisture and temperature distribution, with the pressure being constant throughout at the atmospheric value.

Numerical Strategies Used for the Resolution of the Transport Model. The generalized system of transport equations of the form (Eq. 15) discussed earlier, is discretized by applying the well-known conservative control-volume technique originally devised by Patankar (1980). The equations are integrated over typical rectangular control volumes of the form exhibited in Figure 3.

This type of numerical strategy has been documented in great detail in previously published articles by the present authors (refer to Turner and Perré, 1996). After integrating over each volume within the computational mesh, a system of nonlinear equations result whereby each equation within this system can be cast into a discrete analog of the generalized conservation equation:

$$F_i(\boldsymbol{u}) \equiv \Delta V_i \frac{(\Psi_P^{n+1} - \Psi_P^n)}{\delta t} - \sum_{j=}^{N,S,E,W} \Big[A_{\text{face}_j}^{n+1}(\boldsymbol{u})\Big(\varphi_{w_{Nb_j}}^{n+1} - \varphi_{w_P}^{n+1}\Big) + B_{\text{face}_j}^{n+1}(\boldsymbol{u})\Big(\varphi_{g_{Nb_j}}^{n+1} - \varphi_{g_P}^{n+1}\Big) + C_{\text{face}_j}^{n+1}(\boldsymbol{u})\Big(\omega_{v_{Nb_j}}^{n+1} - \omega_{v_P}^{n+1}\Big) + D_{\text{face}_j}^{n+1}(\boldsymbol{u})\Big(\omega_{a_{Nb_j}}^{n+1} - \omega_{a_P}^{n+1}\Big) + E_{\text{face}_j}^{n+1}(\boldsymbol{u})\Big(\mu_{b_{Nb_j}}^{n+1} - \mu_{b_P}^{n+1}\Big) + F_{\text{face}_j}^{n+1}(\boldsymbol{u})\Big(T_{Nb_j}^{n+1} - T_P^{n+1}\Big)\Big] = 0. \quad (18)$$

The notation used in Eq. 18 is similar to that proposed by Forsyth and Simpson (1991) for the modeling of natural convection in porous media. However, in this work, the nonlinear function $F_i(\boldsymbol{u})$ is a complicated function of the state variable set (S_w, P_w, T, ρ_a, ρ_v, $\bar{\rho}_b$) at the nodes $\boldsymbol{P}$ and all of the neighboring nodes that surround the control volume under consideration. The coefficients $\boldsymbol{A}(\boldsymbol{u})$, $\boldsymbol{B}(\boldsymbol{u})$, $\boldsymbol{C}(\boldsymbol{u})$, $\boldsymbol{D}(\boldsymbol{u})$, $\boldsymbol{E}(\boldsymbol{u})$, and $\boldsymbol{F}(\boldsymbol{u})$ combine the nonlinearities of the kinetics transport coefficients, which involve the state function set at the node $\boldsymbol{P}$ and the four neighboring nodes, together with the relevant geometric factors for the control-volume face. Depending on the particular conservation law being resolved, not all of these coefficients are present in each of the functions F_i. Note that

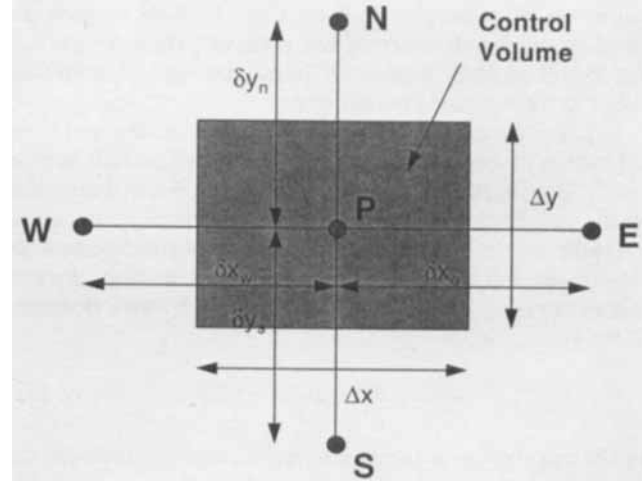

Figure 3. Typical control volume.

the transport coefficients in the terms $A(u)$ and $B(u)$ are *upstream weighted* according to the direction of the liquid- and gas-phase velocities through the control-volume face. All remaining coefficients are averaged according to *arithmetic* averaging techniques.

Once the solution of this system of nonlinear equations has been obtained, the discrete values of the state variables will be known for all control volumes (CVs) within the mesh. For each CV the state variable set (S_w, P_w, T, ρ_a, ρ_v, $\bar{\rho}_b$) is assumed to have an exact definition that can be determined according to the current drying regime. In fact, out of this six-variable set exactly three variables, known as the *primary variables*, will be treated as the unknown independent variables for each CV, and the remaining three variables, known as *secondary variables*, will be computed according to the values of these primary variables. Both the temperature and air density (or total gaseous pressure) are always two of the primary variables no matter in which drying state the process exists; however, the remaining primary variable depends on the state of drying. Furthermore, the values of all variables are presumed to be known at the nth time level. The solution strategy allows these values of the state variables to be advanced correctly to the $(n+1)$-st time level.

By definition for each CV a nonlinear function given by

$$F_i(u_i) = \begin{pmatrix} F_{w_i}(u_i) \\ F_{e_i}(u_i) \\ F_{a_i}(u_i) \end{pmatrix}, \tag{19}$$

where the coordinate functions are, respectively, the three discretized conservation laws and the vector $u_i = (\theta_1^{(i)}, \theta_2^{(i)}, \theta_3^{(i)})^T$ represents the set of three primary variables to be determined from the solution of the three discretized conservation laws for the CV_i, the complete set of N nonlinear functions $\Im(u)$ can be written as

$$\Im(u) = [F_1(u_1), F_2(u_2), F_3(u_3), \ldots, F_N(u_N)]^T. \tag{20}$$

The solution vector u contains N triplets of the three unknown primary variables $\theta_1^{(i)}$, $\theta_2^{(i)}$, and $\theta_3^{(i)}$ that must be determined for each of the N control volumes that define the entire solution domain:

$$u = (u_1 \cup u_2 \cup u_3 \cup \ldots \cup u_N)^T. \tag{21}$$

Since the exact definitions for the primary variables may be different for each CV within the mesh, some careful housekeeping must be maintained throughout the computations.

Finally, in order to obtain values for all state variables at the $(n+1)$-st time level, the system $\Im(u) = 0$ must be resolved. This procedure is carried out in two distinct stages by what are known as *outer* and *inner* iteration phases. During the outer iteration phase, the system of nonlinear equations is linearized according to the complete Newton scheme. The estimate of the solution vector at the $(n+1)$-st level is computed from the current solution at the nth level by writing

$$u^{(n+1)} = u^{(n)} + \delta u^{(n)} \tag{22}$$

and solving the system of linearized equations

$$J(u^{(n)})\,\delta u^{(n)} = -\Im(u^{(n)}) \tag{23}$$

for the correction vector $\delta u^{(n)}$. In Eq. 23, J represents the Jacobian matrix, which is computed numerically as described in Forsyth and Simpson (1991) or Turner and Perré (1996).

During the inner iteration phase the system (Eq. 23) is solved by employing the biconjugate gradient stabilized method (van der Vorst, 1992), together with an incomplete factorization level zero, ILU(0), preconditioning technique (Behie and Forsyth, 1984; D'Azevedo et al., 1992). The combination of Bi-CGSTAB, together with Newton linearization, is a computationally efficient technique for solving the complicated set of drying equations and has been shown in previous research to offer superior convergence rates over the fixed-point outer iteration strategies that are currently being used throughout the drying literature. In fact, the time step, which of course varies during the process, is on average more than 50 times greater and the total computing time between 8 to 20 times lower than the fixed-point equivalent. In general, it was found that the maximum benefits of the Newton strategy were obtained when the most severe transfer conditions were used (Turner and Perré, 1996).

Electromagnetic model

Almost all of the current *state-of-the-art* numerical strategies that resolve problems in electromagnetics use the Maxwell equations as the starting point for their development, since these equations describe adequately an electromagnetic wave that propagates in both time and space:

$$\nabla \times E = -\frac{\partial B}{\partial t}$$

$$\nabla \times H = \frac{\partial D}{\partial t} + \sigma_e E$$

$$\nabla \cdot D = \rho; \qquad \nabla \cdot B = 0$$

$$D = \epsilon E; \qquad B = \mu H \tag{24}$$

In Eqs. 24 the permeability μ, conductivity $\sigma_e = \omega \epsilon_0 \epsilon''$, and permittivity $\epsilon = \epsilon_0 \epsilon'$ are time-independent real quantities that may vary from point to point; and ϵ_0 is the free-space permittivity. In this work, since nonmagnetic materials are being investigated, the permeability is assumed constant at the free-space value $\mu = \mu_0$. Further, because the material under study is wood, the relative dielectric constant $\epsilon'(X,T)$ and the relative dielectric-loss factor $\epsilon''(X,T)$ are assumed to vary with both moisture content and temperature during the drying process. The correlations for ϵ' and ϵ'' utilized throughout this study are taken directly from the literature (Chen and Pei, 1987) and are represented graphically in Figure 4.

Due to the fact that the dielectric-loss factor increases significantly with increasing moisture content, wet zones within the sample of wood are heated directly, and as a consequence, water evaporated more quickly than in dry zones. This moisture-leveling phenomenon provides one of the most important benefits of the process from a quality viewpoint.

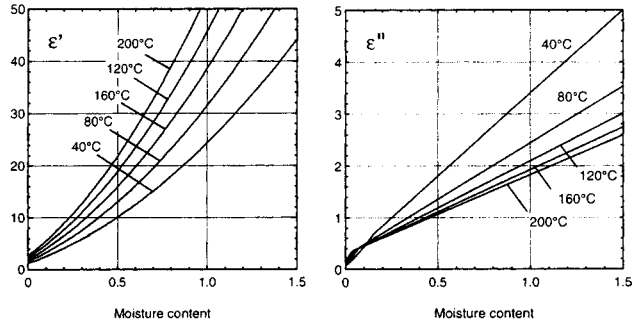

Figure 4. Dielectric properties used in the calculations.

However, again due to the behavior of the loss factor, which often increases with temperature at low moisture contents, a thermal runaway effect can arise at locations where the standing-wave configuration established within the material maximizes. Indeed, this effect is one that is highly undesirable and one that the model describes here, as will be seen in later sections of this work, is able to predict.

The FD-TD method is one of the most popular and widely used numerical methods for predicting dielectric heating phenomena because of its simplicity and ease of implementation. Moreover, this technique can offer fast computation times, and this fact makes it an ideal method for coupling with the complex heat- and mass-transfer model discussed earlier. The FD-TD scheme is second-order accurate in both space and time (De Pourcq, 1985). The scheme proceeds by discretizing the waveguide structure depicted in Figure 1 into elementary YEE cells in which the $\boldsymbol{E}$ and $\boldsymbol{H}$ fields are localized and resolved at alternating half time steps (see Figure 5).

A complete description of the numerical strategy and all of the resulting discretized equations for the six individual field components can be found in previous references; however, as an example, the discrete form of the H_x and E_x components of the electromagnetic fields are presented as follows:

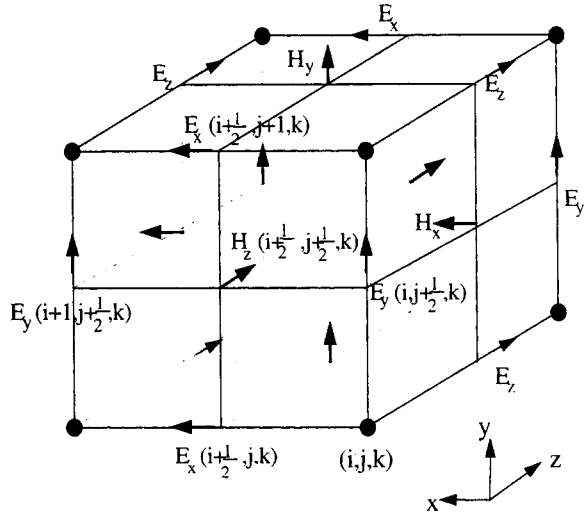

Figure 5. Position of the field components in an *xy*-plane of the Yee lattice.

$$H_x^{n+(1/2)}\left(i,j+\frac{1}{2},k+\frac{1}{2}\right)=H_x^{n-(1/2)}\left(i,j+\frac{1}{2},k+\frac{1}{2}\right)+\tilde{E}_y^n\left(i,j+\frac{1}{2},k+1\right)-\tilde{E}_y^n\left(i,j+\frac{1}{2},k\right)+\tilde{E}_z^n\left(i,j,k+\frac{1}{2}\right)-\tilde{E}_z^n\left(i,j+1,k+\frac{1}{2}\right) \quad (25)$$

$$\tilde{E}_x^{n+1}\left(i+\frac{1}{2},j,k\right)=C_a\left(i+\frac{1}{2},j,k\right)\tilde{E}_x^n\left(i+\frac{1}{2},j,k\right)+C_b\left(i+\frac{1}{2},j,k\right)\left[H_z^{n+(1/2)}\left(i+\frac{1}{2},j+\frac{1}{2},k\right)-H_z^{n+(1/2)}\left(i+\frac{1}{2},j-\frac{1}{2},k\right)+H_y^{n+(1/2)}\left(i+\frac{1}{2},j,k-\frac{1}{2}\right)-H_z^{n+(1/2)}\left(i+\frac{1}{2},j,k+\frac{1}{2}\right)\right], \quad (26)$$

where all symbols and notations are easy to understand and exactly the same as those documented previously in Liu et al. (1994).

Due to the sloped surfaces of the oversized guide, it was decided to use a staircase-type mesh that consisted of only cube-shaped blocks to discretize the domain. Because of the problem symmetry, only half of the domain was computed, and the computational mesh consisted of $18\times yn\times 164$ elements, where yn ranged between 6, for the front and rear waveguides, and 16 for the oversized central section. At $z=z_1$, an input or excitation plane was assumed (see Figure 1). At this plane the FD-TD scheme is corrected for the incident-field components. In order to simulate, respectively, the circulator and the wave trap at either end of the waveguide, an absorbing MUR boundary condition was implemented. The calculation of the power-density distribution within the wood sample requires information about the peak positive and negative excursions of the electric field over each cycle of the incident wave to be observed. Due to the iterative manner in which the electric field and the power density are computed, some form of convergence criterion must be introduced (Liu et al., 1994). For the calculations undertaken here, it was found that between 15 and 25 period cycles were necessary before a smoothly converged power distribution was obtained. The meshes used for the description of the wood sample in the FD-TD and the Transpore models were different, since a more refined mesh was required for the transport calculations, especially close to the exchange surfaces. For the FD-TD, the mesh used $6\times 15\times 11$ elements, while Transpore utilized in the yz-plane a mesh of size 40×20 control volumes, with the size of the control volumes increasing from the exchange surfaces toward the center of the material according to an appropriately chosen geometric progression. In order to couple the two numerical techniques, bilinear interpolation was used to deduce the values of the dielectric properties necessary for FD-TD from Transpore and the power density distribution necessary for Transpore from FD-TD.

Once the microwave source term was coupled to Transpore, the drying process was advanced in time by computing the power-density distribution at short intervals over which either a prescribed heating time had evolved, or the average

moisture content within the sample had changed by at most 2%. This strategy appears to work well and optimizes overall processing time by minimizing the total number of calls to the FD-TD interface. Further, in order to capture the events that transpired during the experiment, the microwave power was turned off once any temperature within the medium exceeded 200°C.

Results and Discussion

Experimental results for heartwood and sapwood

Figures 6 and 7 depict the experimental results for the combined microwave and convective drying of spruce sapwood and heartwood, respectively. The dimensions of the wood sample used for the experiments were 15 cm × 5.5 cm × 3.0 cm, and the magnetron, which is connected to the waveguide, was multicalibrated to deliver incident powers up to 1000 W. However, for the experiments conducted for wood, only incident powers between 100 and 200 W were utilized.

During the microwave experiments four distinct drying periods were identified. In period 1, which is known as the *heating period*, the energy is transferred directly from the microwave field to the wood sample and very little mass loss is incurred. For period 2, known as the *streaming period*, the temperature increases and passes through the boiling point of water, and the resultant large internal vapor pressure drives the liquid from the medium quickly and efficiently under the action of a pumping phenomenon. In fact, this phenomenon was observed during the experiments and for some samples of sapwood it was even possible to determine the amount of liquid that flowed from the endpiece during this phase.

During period 3, which is known as the *enthalpic period*, the moisture content promptly decreases, and under the influence of the elevated internal temperatures, vapor transport becomes the dominant migration mechanism because of the sustained vaporization that is generated within the medium. The final period, known as the *period of thermal runaway*, commences when the medium becomes dry at certain locations and the temperature increases rapidly due to the characteristics of the dielectric-loss factor that were explained in the subsection on the electromagnetic model. During this period, hot spots and consequently, burning, can become evident within the material, eventually resulting in severe product damage. For heartwood, these phenomena were apparent close to the endpiece of the sample (see Figure 7) and, interestingly, the thermal runaway effect was not observed at either the center or at the top surfaces of the board. However, for sapwood (see Figure 6) the thermal runaway appears to be occurring at all three measurement locations.

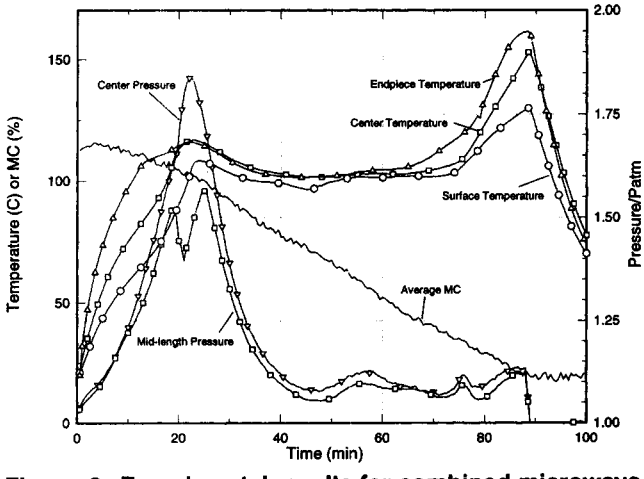

Figure 6. Experimental results for combined microwave and convective drying of spruce sapwood.

Experimental incident power approximately 100 W.

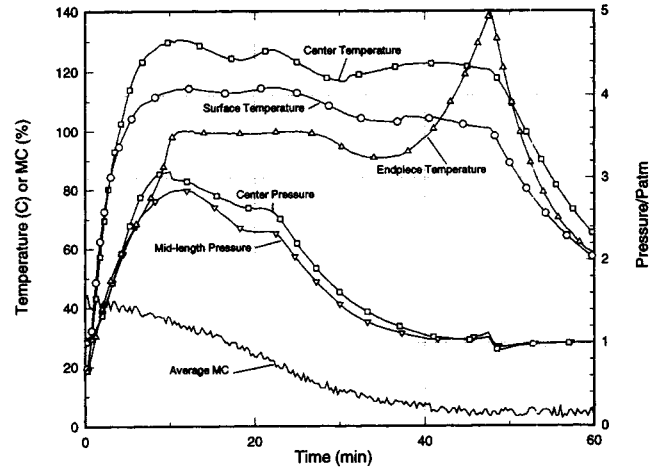

Figure 7. Experimental results for combined microwave and convective drying of spruce heartwood.

Experimental incident power approximately 100 W.

Another observation that can be made from these figures suggests that the internal pressures generated within the wood during microwave-enhanced drying can be quite large. For heartwood the relative pressure peaks at a value of 3, while for sapwood the value is much lower, peaking at around 1.9. Once the microwave power is turned off in order to avoid irrecoverable damage and burning of the sample (see times around 50 min for the heartwood sample and 90 min for the sapwood sample), the temperatures begin to decrease and a small underpressure becomes evident within the medium.

Finally, it can be concluded that the combination of both microwave and convective energies provide an extremely efficient drying process, with the sapwood sample being dried from an initial moisture content of 125% to approximately 10% in less than 100 min, and the heartwood sample being dried from 50% to below 10% in less than 50 min.

Numerical results

The surface area of the excitation port was such that the incident power for the experiment was approximately 2 kW·m^{-2}. The amplitude of the incident electric-field distribution was deduced from the incident power using a classic correlation. The operating frequency was at the microwave level of 2.45 GHz. The input parameters used for the simulations are summarized in Table 2. Note that all of the numerical results presented throughout this section, unless stated otherwise, are recorded for the *yz*-plane located centrally in the wood at the position $x = 1.5$ cm. Only half of the *yz*-plane requires computation due to the symmetry of the microwave system under investigation.

Table 2. Drying Conditions and Initial Material Property Data Used in the Experiment

Drying Conditions and Material Properties	Values Used for the Computations
Initial moisture content	
Sapwood	125%
Heartwood	50%
Initial temperature	30°C
Porosity	0.733
Density of solid matrix	400 $kg \cdot m^{-3}$
Sapwood radial direction:	
Intrinsic liquid permeability	5×10^{-16} m^2
Intrinsic gas permeability	1×10^{-16} m^2
Sapwood longitudinal direction:	
Intrinsic liquid permeability	5×10^{-13} m^2
Intrinsic gas permeability	1×10^{-13} m^2
Heartwood intrinsic permeabilities	Sapwood properties × 0.1
Wood cross section was in the radial and longitudinal directions	5.5 cm × 7.5 cm
Air characteristics	Dry-bulb temperature of 50°C Wet-bulb temperature of 35°C Air velocity of 2 $m \cdot s^{-1}$ Heat-transfer coefficient 15 $W \cdot m^{-2} \cdot K^{-1}$ Mass-transfer coefficient 0.015 $m \cdot s^{-1}$

It is apparent from Figures 8a, 8b, and 9 that the match between the experimental and theoretical results is qualitatively consistent, with the simulation results exhibiting the same overall characteristic shape of the experimental profiles. In fact, perhaps most importantly, the model is able to capture the thermal runaway effects evident within the board for both heartwood and sapwood.

Although there are some differences between theory and experiment, it can be claimed that the coupled complete model developed in this work appears to represent reality more than adequately, signifying that the model can be used as a real tool for investigating in detail this particular drying process at a fundamental level.

Indeed, closer observation of the kinetic curves depicted in Figures 8a and 8b for sapwood verifies that the overall drying time is similar and that the magnitude of the temperatures and pressures predicted within the sample are all close to the experimentally determined values. However, the initial hump in the experimental temperature profiles does not appear in the numerical results. Further, the time of the increase in the numerically computed internal pressure, as well as the complex shape of these curves, does not coincide exactly with what takes place experimentally. This difference could be explained by the actual existence of the percolation pressure inside the medium, which unfortunately, the macroscopic

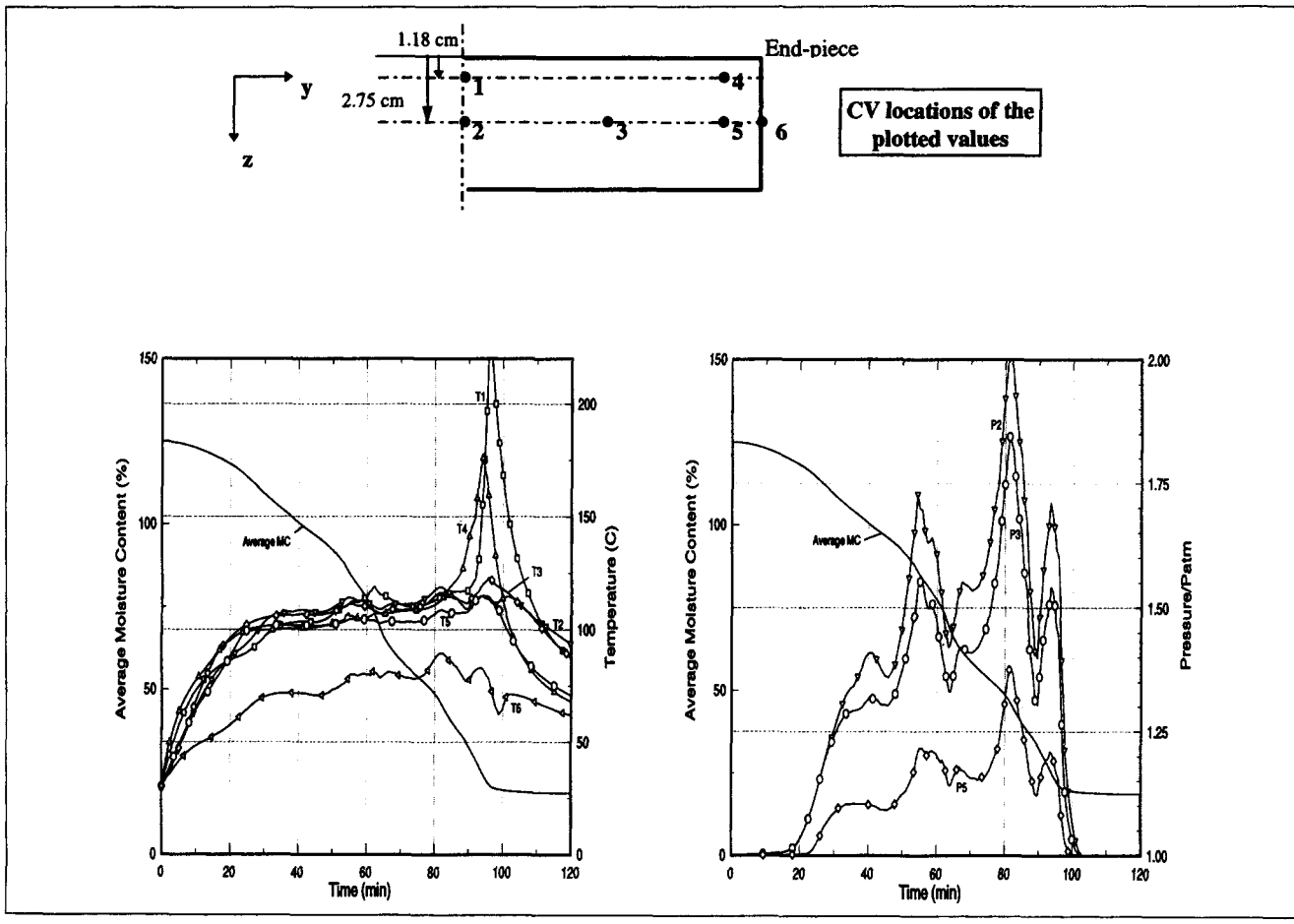

Figure 8. Simulation results for combined microwave and convective drying of spruce sapwood: (a) temperature, and (b) internal pressure.

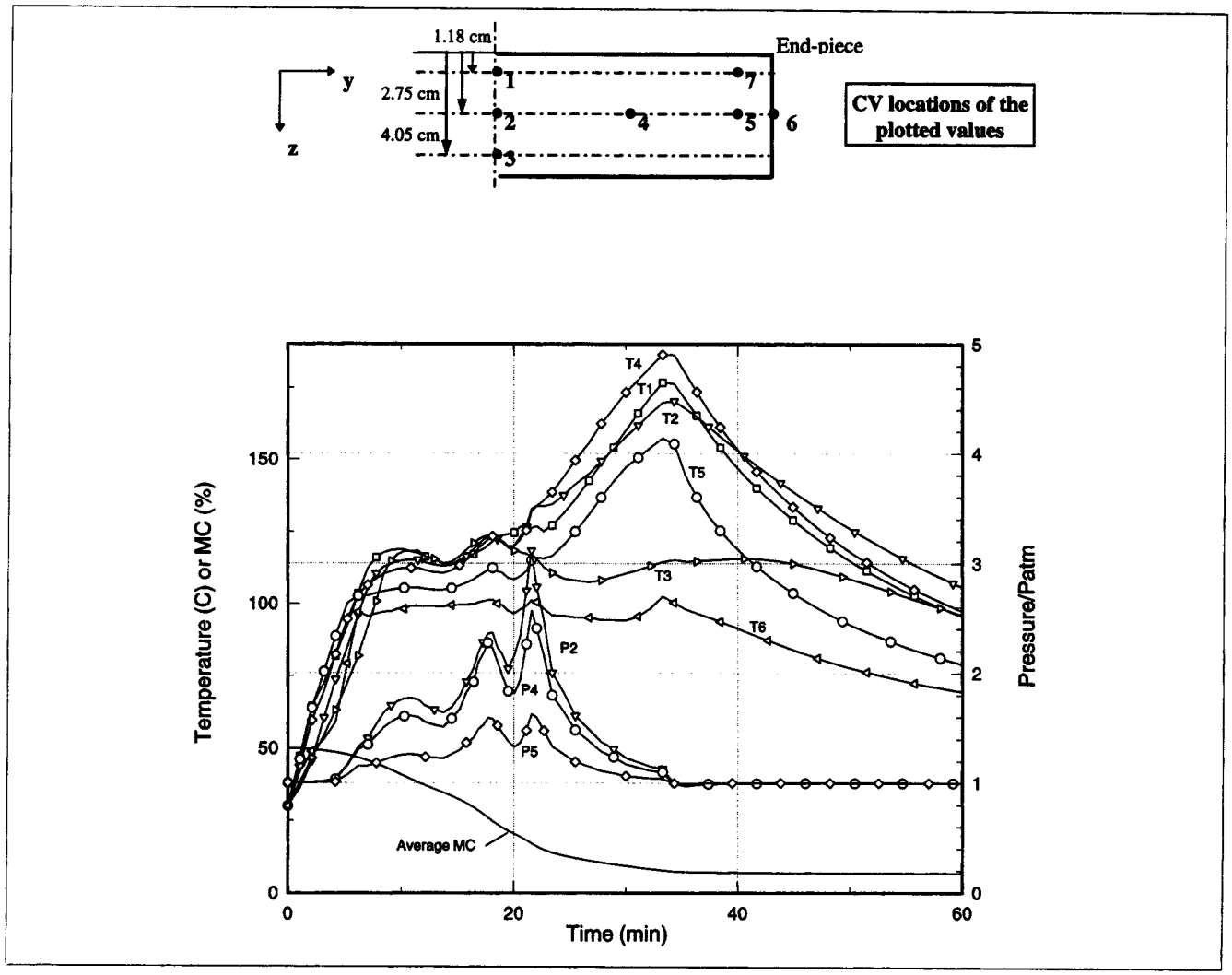

Figure 9. Simulation results for combined microwave and convective drying of spruce heartwood.

model proposed here currently is unable to predict. The numerical simulations also show, as will become more evident from analyzing the three-dimensional surface plots, that the thermal runaway effect for sapwood occurs along the entire interior section of the board located midway between the centerline and the surface.

The results for heartwood are again very promising. Figure 9 highlights that the drying time and the magnitudes of the internal pressure and temperature curves are more consistent with the experimental data than was evident for sapwood. In this case, the computed region where thermal runaway arises within the wood sample appears to align very closely with the experimentally observed position. Note further that the peak in the internal-pressure profiles also is consistent with the experimental results. This improvement is probably explained again by the percolation effect, which is not as critical for heartwood, due to the low initial moisture content and permeability values of the sample.

Another plausible explanation for any differences incurred between theory and experiment concerns the holes that were drilled in the sample for the positioning of the temperature and pressure sensors. Since the vapor is able to move freely along these holes, it is more likely that the sensors will measure the highest pressure and temperature registered throughout the hole, rather than strictly the value at the deepest location. Perhaps it would be more reasonable to take an averaging of the numerical results from the wood center (see, for example, point T2) through to the edge (see T1) when comparing the simulation and experimental results.

General observations of the carpet plots for heartwood and sapwood

Figures 10 and 11 exhibit the tightly coupled phenomena that exist during the combined microwave and convective drying of softwood. These three-dimensional surface plots, which represent snapshots of the drying process at 10, 50, 70 and 90 min for sapwood, and 10, 20, 30 and 40 min for heartwood, show clearly and succinctly the evolution of the combined microwave and convective drying process. The figures are arranged in groups of four and ordered according to (1) *the power density*, which influences the heating phenomena, (2) *the temperature*, which in turn impacts the internal vapor pressure; (3) *the pressure*, which determines the shape of the

moisture profiles, and finally (4) *the moisture* distributions, which affects the power distribution.

Observations for Sapwood. An analysis of the sapwood profiles in Figures 10a and 10b show that after 10 min of heating, the temperature in the section of the board situated closest to the incoming electromagnetic waves, heats up to the boiling point at a faster rate than is apparent anywhere else within the board. Nevertheless, the liquid profiles within the wood remain fairly uniform and the internal pressure rests close to the atmospheric value throughout this period. At 50 min, it is possible to observe the real impact that the anisotropy of the wood has on the drying process, with liquid being driven quickly toward the endpiece of the board, the evidence of a large trough in the moisture profile and a rapid increase in the internal overpressure at the hottest location within the wood. Furthermore, there is a pronounced complex wave pattern arising in the power-density profiles.

As the drying process proceeds, it is possible to detect a moisture leveling effect within the sample. In fact, the rapid internal vaporization pumps the liquid from the interior of the board toward the surface, culminating in a shift in the phase and a change in the amplitude of the propagating waves. It is also possible to recognize the saturated endpiece phenomenon for sapwood that is a trademark of high-temperature drying. However, in this case, the saturation profile has a rather unusual shape associated with it.

At 90 min, just prior to turning off the microwave source, the hot spot close to the endpiece can be observed clearly, along with further evidence of moisture leveling. In fact, the combination of moisture leveling and rapid internal vaporization cause a change in the location of the maximum pressure to occur. The internal pressure now appears largest close to the trailing edge of the board, which is the region where there is the most liquid. The power density is now displaying an even more distinct shape than was evident earlier in the drying process, clearly maximizing around the wettest locations

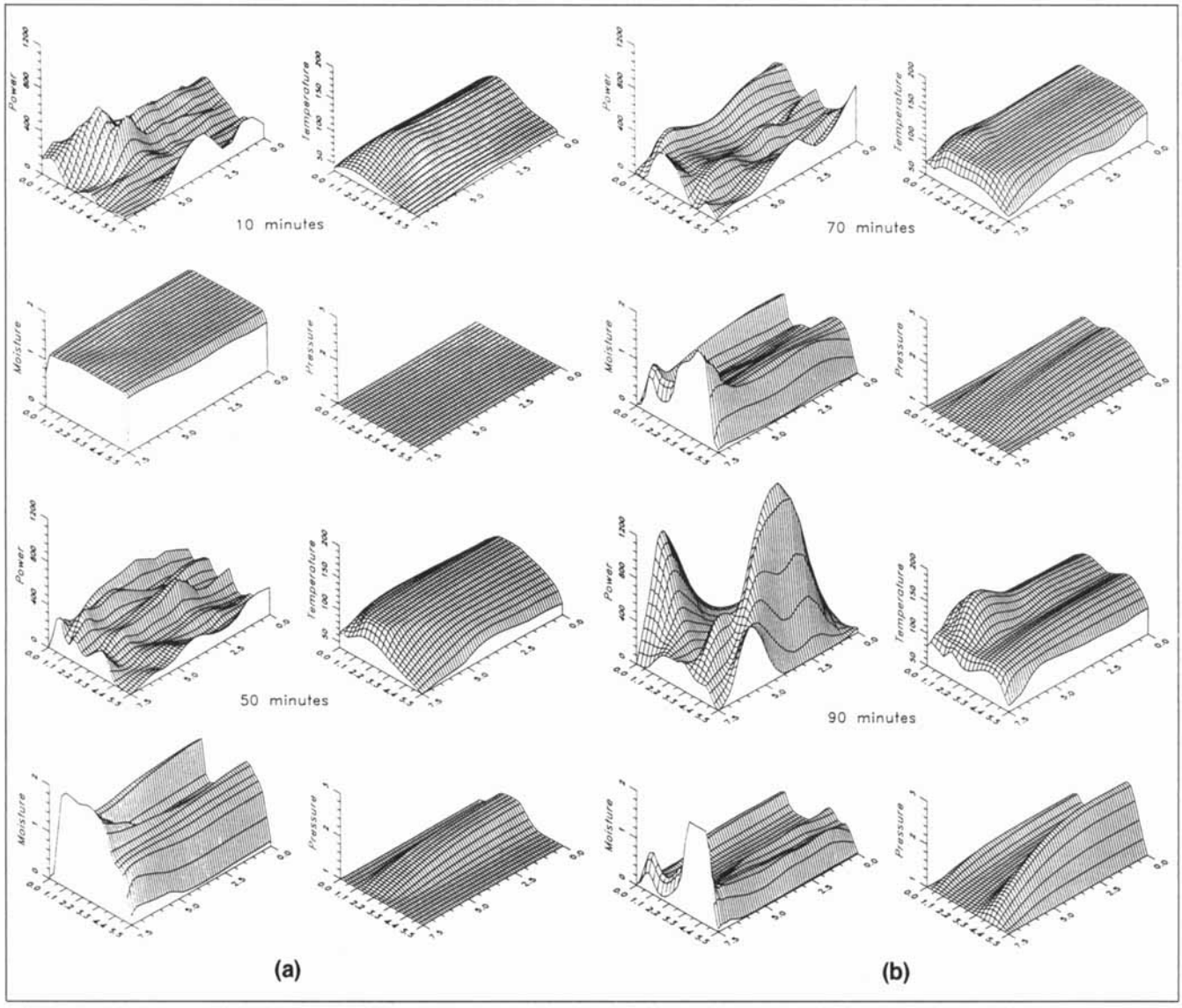

Figure 10. Carpet plots of the power density, temperature, pressure, and moisture content distributions: (a) 10 and 50 min for sapwood; (b) at the times 70 and 90 min for sapwood.

of the board. The unusual shape of the endpiece saturation profile is exacerbated during this heating period, being influenced strongly by the internal-pressure profiles.

Due to the large initial moisture content, the skin-depth heating effect causes a majority of the microwave power to be reflected during the early irradiation phase. This phenomenon explains why the amplitude of the power density for sapwood is slightly lower than that observed for heartwood and why the heating is more intense close to the leading edge of the sapwood sample.

Eventually, after a majority of this liquid is expelled from the wood, the microwaves can penetrate further into the material and the heating becomes more volumetric. During this period, the behavior of the dielectric properties is influenced primarily by that of free water. After the energy is turned off, a reasonably large proportion of moisture appears to remain close to the trailing edge of the board. The temperature and pressure begin to fall back to the conditions that are established due to the drying-air characteristics. It could be argued that the microwave power source could be turned back on at this stage in order to assist with the leveling of the residual moisture.

In summary, it is clear that the physics responsible for producing the rather smoothly behaved drying kinetics curves exhibited in Figures 8 are indeed very complex and interlinked. In fact, the simulation results presented in the form of the three-dimensional graphics are able to provide a far better insight of the entire process than could ever be imagined from the drying kinetic curves. The power of the mathematical model should now be well recognized—it is felt that the developed model can be used with confidence for identifying and increasing the knowledge of the way in which microwaves interact with wet porous hygroscopic and anisotropic materials, such as wood, throughout combined microwave and convective drying.

Observations for Heartwood. It is possible to observe from Figures 11a and 11b that for heartwood the board dries quickly throughout, without the endpiece saturation phenomenon that arises for sapwood. In particular, the region of the board that receives the largest amount of microwave en-

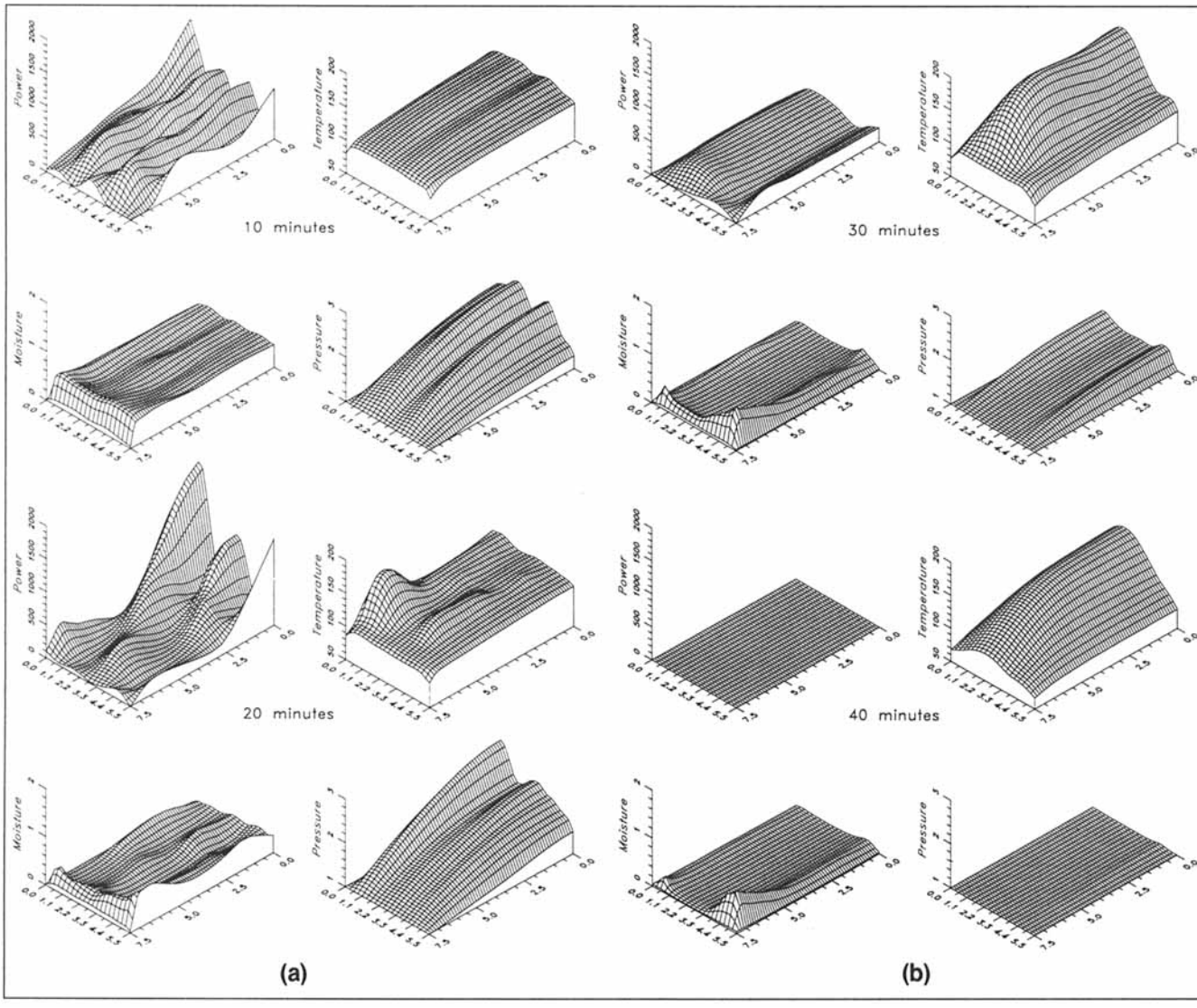

Figure 11. Carpet plots of the power density, temperature, pressure, and moisture content distributions: (a) 10 and 20 min for heartwood; (b) at the times 30 and 40 min for heartwood.

ergy in the early stages of the process, due to the penetration depth of the microwave field, heats rapidly, and at 20 min the evidence of a hot spot in the wood close to the endpiece can be seen clearly. At 30 min the temperatures around this location highlight the effect of thermal runaway, since it is this section of the board that is now the driest.

Examination of the power-density profiles allows a complicated wave behavior within the sample to be detected, especially in the center of the material where its shape is the most pronounced. This behavior develops as a direct result of the external traveling-wave field and the abrupt changes in the effective loss factor, which varies with the history of the moisture and temperature fields that have evolved in time before it. This waveform can also incite a wavelike phenomenon to arise in both the internal pressure and moisture profiles across the radial direction of the sample. The effect of the anisotropy of the wood plays an important role with the determination of the shape and magnitude of each of these distributions.

Once the power is turned off (see Figure 11b) at 40 min, the temperature field begins to reduce in magnitude and the strong overpressure that was evident earlier in the drying process returns to the atmospheric value.

Finally, a more general comment concerning the power-density profiles for both sapwood and heartwood pertains to the effect of the initial moisture content on the shape and amplitude of the power distribution. The sapwood sample, which has a high initial moisture content and is more permeable than heartwood, induces a power-density profile that displays a quite complex and multimodal wavelike behavior. Heartwood, on the other hand, which has a low initial moisture content and is not as permeable as sapwood, presents a power-density distribution exhibiting a more consistent monowavelike behavior typical of what is likely to be observed within an oversized waveguide. These effects are no doubt a direct result of the characteristics of the dielectric properties of the two different sample types. Sapwood, due to the large volume of free water contained within, behaves like a highly lossy material, while heartwood, influenced by the behavior of the dielectric properties of the bound liquid within the cell walls of the wood, behaves like a low lossy material.

Need for a Complete Three-Dimensional Model

At this stage it can be seen from the results presented throughout the previous sections of this work, that the match between experimental and theoretical results are reasonable. However, it is still unclear what the impact of using a two-dimensional heat- and mass-transfer model, coupled with a three-dimensional electromagnetic-field computational model, can have on the overall simulation results. Furthermore, the importance of the three-dimensional heating effects within this type of microwave system have not been studied. To elucidate on these issues, the model was run again with the heat- and mass-transfer model computed according to the heating phenomena that are generated in the top section of the board, at the position $x = 3$ cm, rather than at the center of the board at $x = 1.5$ cm. The results of this trial are presented in the following section.

Recall further that the exact configuration used for the experiments required that the wood sample be sealed entirely by resin along the trailing edge xy-plane. To investigate the effect of imposing such a boundary condition within the model proposed in this text, the heartwood and sapwood cases were recomputed allowing only heat to be transferred through this resin plane—absolutely no mass transfer was permitted. All other parameters remained unchanged and the results of this study are described in the subsection on the effect of using the resin coating at the board's trailing edge.

Study of the results computed for the top section of the board

The results in Figure 12 depict the overall drying kinetics for the top section of the board during the combined microwave and convective drying of heartwood. In general, when comparing Figure 12 with Figure 9, it can be seen that although the trends in the drying characteristics are similar in both cases, the top section of the board requires a much longer drying time than the core section. Furthermore, the internal temperatures and pressures are lower for the top section than for the central section. The findings of this short study show that the geometry of the microwave applicator does cause a completely three-dimensional heating distribution to be generated within the sample during the drying process. It can be concluded that great care must be taken when using this type of model (two-dimensional heat and mass transfer and three-dimensional electromagnetic heating) to analyze all aspects of the drying phenomena that are produced by such a complicated and convoluted process. Unfortunately, some of the three-dimensional heating phenomena are not identified completely by studying only the heat and mass transfer in a single yz-plane cross section of the wood sample. Obviously, the next stage in this research concerns the development of a three-dimensional heat- and mass-transfer code. Current research impetus is being focused by the authors on the tedious task of implementing such a code.

Study of the effect of using the resin coating at the trailing edge of the board

Figures 13 and 14 show the effect of using the resin boundary condition within the model for both sapwood and heartwood, respectively. The results for sapwood appear similar to

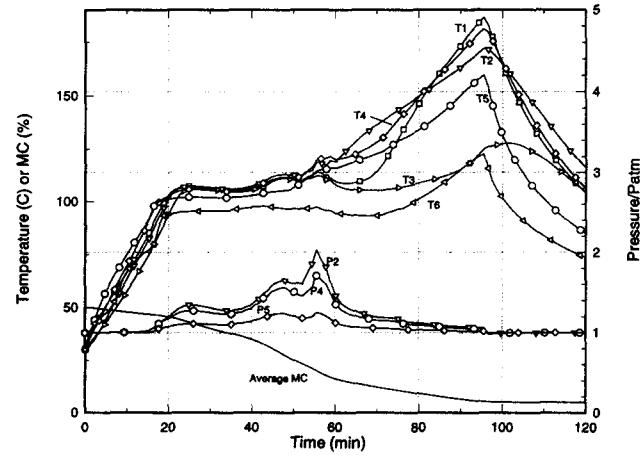

Figure 12. Heartwood kinetics computed for the top surface of the board.

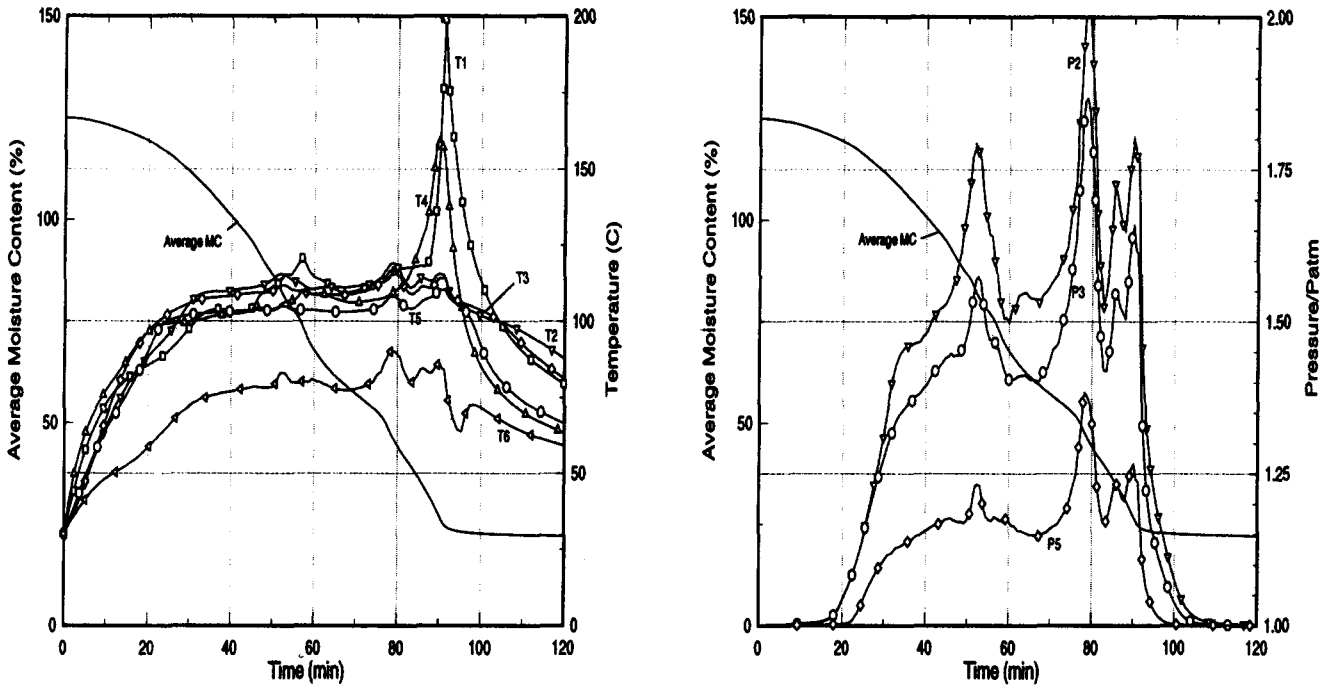

Figure 13. Impact of using the resin coating on the two-dimensional drying results for sapwood.

the case where the trailing edge of the board is treated as a drying surface (see Figure 8). Nevertheless, there are some differences, and a closer comparison between the two cases highlights that the drying time is reduced, the temperatures are lower, and the internal pressures have a slightly different shape for the resin boundary case.

It appears that, again due to the skin-depth phenomenon, a majority of the microwave energy is reflected from the surface of the wood sample as a result of the sapwood high internal moisture content. In this case, the anisotropy of the sample coupled with the edge heating effects play an important role in the free liquid mass migration from the center of the board toward the endpiece of the sample. The resin boundary tends to have little impact on the sapwood drying process as a whole.

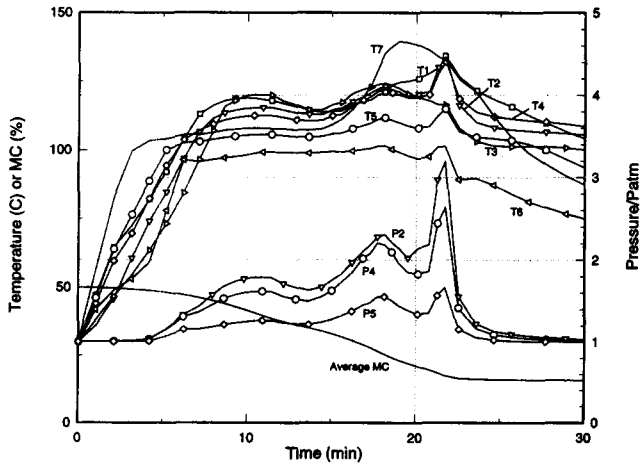

Figure 14. Impact of using the resin coating on the two-dimensional drying results for heartwood.

For heartwood, the effect of the resin boundary is far more noticeable than was evident for sapwood. The drying time is much faster, higher internal temperatures arise, and a far more pronounced power distribution is generated within the material for the resin case as opposed to the results given in Figure 9 for the drying surface boundary case. These effects can be studied in more detail from the three-dimensional surfaces given in Figure 15 after 20 min of drying. It seems that the water buildup around the trailing edge of the material acts somewhat like a reflective or conducting surface, causing an amplification of the heating phenomena within the material. Again, these phenomena are due to the microwave penetration depth, which of course is much higher for heartwood due to the lower initial moisture content. The results obtained here emphasize again the real three-dimensional heating effects generated throughout the experiments. Although for sapwood, the results remain fairly consistent with the experiments when the resin boundary is imposed within the model, in the general case, the impact of preventing mass transfer at the trailing edge can cause significant differences in the drying kinetics. It seems unrealistic to insulate only one among four of the drying surfaces in the model, when one in six is insulated during the experiment. These differences highlight the need for developing a complete three-dimensional model.

Conclusions

Bearing in mind the complicated physics that arise during microwave-assisted drying processes, as well as understanding the limitations of the proposed theory, it can be concluded that the results presented in this work are more than satisfactory. The model, which combines a two-dimensional transfer code with a three-dimensional electromagnetic com-

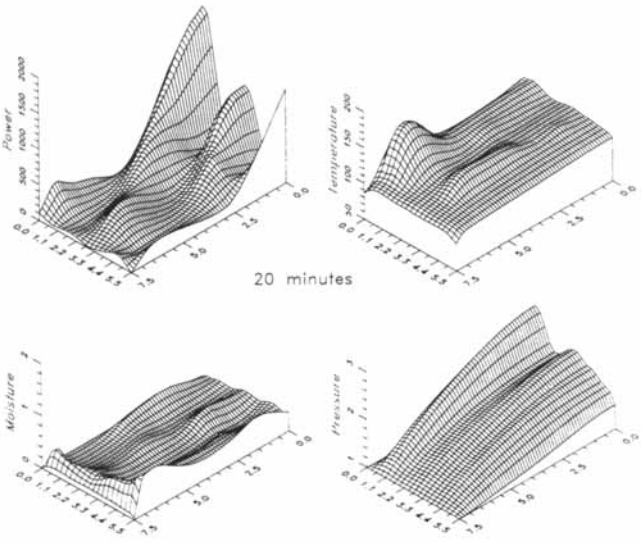

Figure 15. Carpet plot for heartwood after 20 min of drying when the resin boundary condition is imposed within the model.

putational scheme, captures the overall drying behavior reasonably well. Most importantly, the developed model is able to predict the occurrence of hot spots and thermal runaway within the material. This model can now be used as a cognitive tool for studying in detail the combined microwave and convective drying process. The aim of such a tool is not only to provide a good evaluation of different waveguide geometries and designs, but for identifying any relations that may exist between the heating phenomena established by the applicator and the size and shape of the product being heated. Further, the model can be used to increase the awareness of how electromagnetic fields interact with complicated wet porous materials such as wood. It is hoped that the results of this fundamental analysis on combined microwave and convective drying of softwood will be deliberated by drying technicians so that the information disseminated throughout this text can be utilized to steer microwave technology toward the leading role in the industrial drying sector that it deserves to achieve.

The concluding remarks for this work must emphasize the real need for developing a completely three-dimensional model. Previous work on the drying model proved that at least a two-dimensional model was necessary if the heat- and mass-transport phenomena that arise in high-temperature convective drying of wood are to be captured adequately. This fact was motivated by the longitudinal transfer that was established as a result of the internal overpressures generated within the board. Obviously, the electromagnetic heating of a highly anisotropic medium induces fundamentally three-dimensional phenomena. It must be kept in mind that some of the particular phenomena generated during the microwave drying process, unfortunately, can escape the model combination presented in this work. The next stage in the evolution of this research concerns the development of a three-dimensional heat- and mass-transfer code, and the impetus of current research is being focused by the authors on this tedious task.

Acknowledgments

One of the authors, Ian Turner, thanks CSR Softwoods, Queensland Pty. Ltd. of Australia for their continuing support of this work. He also thanks the ENGREF for supporting his sabbatical stay in Nancy, France. Both authors thank Prof. Roques for allowing the use of the oversized waveguide to perform the experiments. Some of the computations referred to in this article were carried out on computing equipment supplied to the School of Mathematics, Queensland University of Technology, under the Digital Equipment Agreement ERP No. 2057. This work was also supported by an ARC Collaborative Research Grant scheme from the Australian Government.

Notation

$\boldsymbol{B}$ = magnetic flux intensity, T
c = speed of light in vacuum, $m \cdot s^{-3}$
c = molar concentration, $mol \cdot m^{-3}$
C_p = specific heat, $J \cdot kg^{-1} \cdot K^{-1}$
$\boldsymbol{F}_i(\boldsymbol{u}_i)$ = vector nonlinear function for each CV
$\mathfrak{F}(\boldsymbol{u})$ = complete set of nonlinear functions
g = gravitational constant, $m \cdot s^{-2}$
h = intrinsic averaged enthalpy, $J \cdot kg^{-1}$
$\bar{h}$ = averaged enthalpy of bound liquid, $J \cdot kg^{-1}$
h^0_{vap} = latent heat of evaporation, $J \cdot kg^{-1}$
Δh_w = differential heat of sorption, $J \cdot kg^{-1}$
$\boldsymbol{H}$ = magnetic-field vector, $A \cdot m^{-3}$
$\underline{\underline{\boldsymbol{K}}}_{\text{eff}}$ = effective thermal conductivity, $W \cdot m^{-1} \cdot K^{-1}$
$\underline{\underline{K}}$ = relative permeability
$\underline{\underline{k}}$ = absolute permeability, m^2
M = molar mass, $kg \cdot mol^{-1}$
$\boldsymbol{n}$ = unit normal
P_{inc} = incident power, $W \cdot m^{-2}$
R = gas constant, $J \cdot mol^{-1} \cdot K^{-1}$
S = volume saturation
t = time, s
$\boldsymbol{v}$ = velocity, $m \cdot s^{-1}$
V = averaging control volume
X = moisture-content dry basis
X_{FSP} = fiber saturation point
y = longitudinal direction
z = transverse direction
δt = discrete time step
ΔV = discrete volume of CV
ϕ = porosity, $m^3 \cdot m^{-3}$
μ = dynamic viscosity, $kg \cdot m^{-1} \cdot s^{-1}$
ρ = intrinsic averaged density, $kg \cdot m^{-3}$
σ = Stefan Boltzmann constant, $W \cdot m^{-2} \cdot K^{-4}$
ω = mass fraction
ω = relaxation factor
ω = frequency, Hz

Superscripts and subscripts

a = air
c = capillary
FSP = fiber saturation point
g = gas phase
i = general index for vectors
Nb = neighboring CV point
p = pressure
P = CV centroid point
R = reference
s = solid phase
T = temperature
1 = initial value

Literature Cited

Behie, G., and P. A. Forsyth, "Incomplete Factorization Methods for Fully Implicit Simulation of Enhanced Oil Recovery," *SIAM J. Sci. Stat. Comput.*, **5**, 543 (1984).

Bird, R. B., W. E. Stewart, and E. N. Lightfoot, *Transport Phenomena*, Wiley, New York (1960).

Bonneau, P., "Modélisation du séchage d'un matériau hétérogène: application à un bois de résineux," Thèse de l'université Bordeaux I, Bordeaux, France (1991).
Chen, P. S., and D. C. T. Pei, "Microwave Heating in Drying of Hygroscopic Materials," *IEEE MONTECH*, p. 72 (1987).
Constant, T., "Le Séchage Combiné Convection-Micro-Ondes: Modélisation–Validation–Optimisation," Thèse l'Institut National Polytechnique de Lorraine, Lorraine, France (1992).
Constant, T., P. Perré, and C. Moyne, "Drying with Internal Heat Generation: Theoretical Aspects and Application to Microwave Heating," *AIChE J.*, **42**(2), 359 (1996).
Couture, F., "Modélisation Fine d'un Probléme de Séchage: Développement d'Outils Adaptés," Thèse de l'université Bordeaux I, Bordeaux, France (1995).
D'Azevedo, E. F., P. A. Forsyth, and W. P. Tang, "Towards a Cost Effective ILU Preconditioner with High Level Fill," *BIT*, **32**, 442 (1992).
De Pourcq, M., "Field and Power-Density Calculations in Closed Microwave Systems by Three-Dimensional Finite Differences," *IEEE Proc. H, Microwaves, Opt. & Antennas*, **132**(Part H, 6), 360 (1985).
Forsyth, P. A., and R. B. Simpson, "A Two-Phase, Two-Component Model for Natural Convection in a Porous Medium," *Int. J. Numer. Methods Fluids*, **12**, 655 (1991).
Jolly, P. G., and I. W. Turner, "A Theory of Microwave and Convective Drying," *Technol. Today* (Czechoslovak Academy of Sciences), **5**, 273 (1991).
Liu, F., and I. W. Turner, "Numerical Modelling Techniques for Simulating the Microwave Heating or Polymer Materials Inside a Ridge Waveguide," *Proc. Biennial Conf. on Computational Techniques and Applications: CTAC* World Scientific Publishing, p. 514 (1995).
Liu, F., I. W. Turner, and M. E. Bialkowski, "A Finite-Difference Time-Domain Simulation of the Power Density Distribution in a Dielectric Loaded Microwave Cavity," *J. Microwave Power Electromagn. Energy*, **29**(3), 138 (1994).
Liu, F., I. W. Turner, E. Siores, and P. Groombridge, "A Numerical and Experimental Investigation of the Modelling of the Microwave Heating of Polymer Materials Inside a Ridge Waveguide," *J. Microwave Power Electromagn. Energy*, **31**(2), 71 (1996).
Pang, S., R. B. Keey, and T. A. G. Langrish, "Modelling the Temperature Profiles within Boards during the High Temperature Drying of Pinus Radiata Timber," *Drying '92*, A. S. Mujumdar, ed., Elsevier, p. 417 (1992).
Patankar, S. V., *Numerical Heat Transfer and Fluid Flow*, McGraw Hill, New York (1980).
Perré, P., and A. Degiovanni, "Simulation par volumes finis des transferts couplés en milieux poreux anistropes: séchage du bois à basse et à haute température," *Int. J. Heat Mass Transfer*, **33**(11), 2463 (1990).
Perré, P., M. Moser, and M. Martin, "Advances in Transport Phenomena During Convective Drying with Superheated Steam or Moist Air," *Int. J. Heat Mass Transfer*, **11**(36), 2725 (1993).
Perré, P., "Drying with Internal Vaporization: Introducing the Concept of Identity Drying Card," *Drying Technol. J.*, **13**(5–7), 1077 (1995).
Perré, P., and I. W. Turner, "The Use of Macroscopic Equations to Simulate Heat and Mass Transfer in Porous Media: Some Possibilities Illustrated by a Wide Range of Configurations that Emphasis the Role of Internal Pressure," *Mathematical Modeling and Numerical Techniques in Drying Technology*, I. W. Turner and A. Mujumdar, eds., Dekker, New York, p. 83 (1996).
Perré, P., "Image Analysis, Homogenization, Numerical Simulation and Experiment as Complementary Tools to Enlighten the Relationship Between Wood Anatomy and Drying Behaviour," *J. Drying Technol.*, in press (1997).
Puiggali, J. R., and M. Quintard, "Détermination de Propriétés de Transfert dans les Strates d'un Bois Résineux," *CR Acad. Sci. Paris*, Ser. II, **310**, 1719 (1990).
Stanish, M. A., G. S. Schajer, and F. Kayihan, "A Mathematical Model of Drying for Hygroscopic Porous Media," *AIChE J.*, **32**(8), 1301 (1986).
Turner, I. W., and P. G. Jolly, "The Effect of Dielectric Properties on Drying Kinetics," *J. Microwave Power Electromagn. Energy*, **25**(4), 212 (1990).
Turner, I. W., "The Modelling of Combined Microwave and Convective Drying of a Wet Porous Material," PhD Thesis, Dept. of Mechanical Engineering, The Univ. of Queensland, Brisbane, Australia (1991).
Turner, I. W., and P. G. Jolly, "Combined Microwave and Convective Drying of a Porous Material," *J. Drying Technol.*, **9**(5), 1209 (1991).
Turner, I. W., "A Two-Dimensional Orthotropic Model for Simulating Wood Drying Processes," *J. Appl. Math. Modelling*, **20**, 60 (1996).
Turner, I. W., and P. Perré, "A Comparison of the Drying Simulation Codes TRANSPORE and WOOD2D Which are Used for the Modelling of Two-Dimensional Drying Processes," *J. Drying Technol.* (Special Ed. on *Mathematical Modelling and Numerical Simulation*), **13**(3), 695 (1995).
Turner, I. W., and P. Perré, "A Synopsis of the Strategies and Efficient Resolution Techniques Used for Modelling and Numerically Simulating the Drying Process," *Mathematical Modeling and Numerical Techniques in Drying Technology*, I. W. Turner and A. Mujumdar, eds., Dekker, New York, p. 1 (1996).
van der Vorst, H. A., "Bi-CGSTAB: A Fast and Smoothly Converging Variant of Bi-CG for the Solution of Nonsymmetric Linear Systems," *SIAM J. Sci. Stat. Comput.*, **13**, 631 (1992).
Whitaker, S., "Simultaneous Heat, Mass and Momentum Transfer in Porous Media: A Theory of Drying," *Advances in Heat Transfer*, Vol. 13, Academic Press, New York, p. 119 (1977).

Manuscript received Dec. 30, 1996, and revision received May 9, 1997.